ADVANCED FUNCTIONAL MATERIALS
www.afm-journal.de

Understanding the Critical Role of Binders in Phosphorus/Carbon Anode for Sodium-Ion Batteries through Unexpected Mechanism

Wei Xiao, Qian Sun, Mohammad Norouzi Banis, Biqiong Wang, Weihan Li, Minsi Li, Andrew Lushington, Ruying Li, Xifei Li, Tsun-Kong Sham, and Xueliang Sun**

Polymer binders that combine active materials with conductive agents have played a critical role in maintaining the structural integrity of phosphorus anodes with a huge volume change upon sodiation/desodiation. Herein, the role of binders on the structural/chemical stability of phosphorus/carbon anode is spectroscopically uncovered through unexpected mechanism. Surprisingly, the selection of different binders is found to determine the oxidation degree of active phosphorus in various electrodes, which correlate well with their electrochemical properties. At a high oxidation degree, the electrode applying a conventional poly(vinylidene difluoride) binder displays the worst electrochemical properties, while the electrode using a sodium alginate binder delivers the best electrochemical performance (a highly reversible capacity of 1064 mAh g^{-1} with a 90.1% capacity retention at 800 mA g^{-1} after 200 cycles and an outstanding rate capability of 401 mAh g^{-1} at 8000 mA g^{-1}) for its negligible oxidation. Additionally, the emergence/decomposition of surface intermediates, including $(PO_2)^{3-}$ and $(PO_4)^{3-}$ species, are observed in the discharging/charging processes via the ex situ P K-edge X-ray absorption spectroscopies. This novel discovery of the unique role of binders in phosphorus anodes, not only provides an opportunity to ameliorate their electrochemical properties, but also enables their practical applications in high-energy sodium-ion batteries.

1. Introduction

The industrialization of lithium-ion batteries (LIBs) with a high energy density and an inherent safety, has commercialized the portable electronics and enabled the applications of electrical vehicles (EVs). However, the profound uncertainty on the limited lithium resources in remote areas and their subsequently soaring prices in recent years, hindered the future applications of LIBs.[1] Sodium-ion batteries (SIBs) with natural abundance and environmental benignity, have been frequently revisited as promising candidates for energy storage in the large-scale applications.[2] As the elemental sodium is located in the same group of periodic table as lithium, SIBs have inherited the similar reaction mechanisms from lithium-based batteries, involving sodium intercalation/alloying/conversion and the analogous physicochemical properties including the larger ionic size of Na^+ compared with Li^+ (1.02 vs 0.76 Å).[3] Even though the sluggish kinetics regarding a poor Na^+ diffusion rate and structural instability of host during a huge volume change severely limited the specific energy densities and cycle durability of SIBs, their significant advantage in cost effectiveness further promised the potential applications in the stationary grid energy storage and intermittent renewable energy storage.[4]

However, the absence of a suitable anode restricts the practical development of SIBs. Graphite, known as a typical layer-structured anode in LIBs, cannot be utilized for SIBs in conventional carbonate-based electrolyte, owing to the thermodynamically unfavorable formation of Na-graphite intercalated compounds.[5] Although the ether-based electrolyte could boost the electrochemical properties of carbon anodes, the reversible capacities are still low.[6] While the sodium metal has severe safety issues involving its low melting point (97.7 °C) and the inevitable dendrite growth upon repeated cycling,[3c] disordered carbon materials with the increased interlayer distances and more electrochemically active sites for sodium storage, presented highly reversible capacities around 300 mAh g^{-1} but with poor rate capabilities.[7] Even the well-established

Dr. W. Xiao, Dr. Q. Sun, Dr. M. N. Banis, Dr. B. Wang, Dr. W. Li, M. Li, Dr. A. Lushington, R. Li, Prof. X. Sun
Department of Mechanical and Materials Engineering
The University of Western Ontario
London, Ontario N6A 5B9, Canada
E-mail: xsun9@uwo.ca
Dr. W. Xiao, Prof. T.-K. Sham
Department of Chemistry
The University of Western Ontario
London, Ontario N6A 5B7, Canada
E-mail: tksham@uwo.ca
Dr. W. Xiao, Prof. X. Li
Institute of Advanced Electrochemical Energy
School of Materials Science and Engineering
Xi'an University of Technology
Xi'an, Shaanxi 710048, China
The ORCID identification number(s) for the author(s) of this article can be found under https://doi.org/10.1002/adfm.202000060.

DOI: 10.1002/adfm.202000060

nanotechnologies were applied to tailor the electrochemical properties of carbon materials, the electrochemical performances cannot meet the application requirements of highly durable and affordable SIBs.[8] It is urgently necessary to develop high-capacity, long-life, and low-cost anode materials with a superior electrochemical performance.

Phosphorus, based on an alloying reaction of 1 phosphorus with 3 sodium per atom, has emerged as an ideal anode material, which possesses a highest theoretical capacity of 2596 mAh g^{-1} and a desirable working voltage plateau of 0.1–0.6 V, yielding a very high energy density.[9] Generally, there are four different allotropes of phosphorus, including red, black, white, and violet, each with strikingly different physicochemical properties. The white phosphorus is highly pyrophoric and flammable, while the violet and black phosphorus are difficult to synthesize with the stringent requirements for an ultralong heating. Therefore, the commercially available and relatively stable red phosphorus is generally considered as a best choice of anode material for SIBs.[10] Unfortunately, its low electronic conductivity (≈10^{-14} S cm^{-1}) triggered an obvious electrochemical polarization and a low utilization of active materials.[11] Worsely, the huge volume expansion/shrinkage (292%) for red phosphorus in the repeated sodiation/desodiation processes, gradually resulted in the structural collapse and subsequent pulverization for active materials along with a fast capacity degradation. To circumvent these challenges, the porous carbon is homogeneously mixed with red P to facilitate the electron/ion migrations and buffer the large volume changes.[9e–g,10,12]

The fabrication of phosphorus/carbon (P/C) composites either involved the mechanical-milling or vaporization-condensation route. The mechanical-milling approach, including hand-grinding and machine-milling processes, was employed to reduce the particle size of red P and mix it with the porous/conductive carbon materials (carbon black,[9e–g,12a,13] carbon nanotubes,[12b,14] graphene,[12c–f,15] 3D carbon,[12g,16] composite[12h]). Particularly, the carbon material would remarkably ameliorate the insulative nature of red P and further cushion the large volumetric change of phosphorus anodes upon cycling. The vaporization-condensation method, initially sublimated the solid of red P above 450 °C and naturally dispersed the phosphorus vapor during condensation by capillary force and pressure difference into the robust/conductive carbon matrix (porous carbon,[10,12i] carbon nanofibers,[12j,k] carbon nanotubes,[12l,17] mesoporous carbon,[12m,18] MOF-derived microporous carbon,[12n,19] hierarchical porous carbon,[20] biomass carbon,[21] graphene paper[12o] and aerogel[12p]), which could accommodate the huge volume variations upon the sodiation/desodiation processes and provide the abundant channels for ion diffusion as well as electron transport.

Typically, a sodium-ion battery was composed of a cathode, and an anode with a separator between them in the electrolyte, and the electrode consisted of an active material, a conductive agent, and a polymer binder. In terms of component functionality, the active material determines the basic electrochemical properties, while the conductive agent ameliorated the electronic conductivity. A polymer binder was utilized to bond the active material and conductive agent together with current collector, facilitating the electron transport and ion diffusion.[22] For phosphorus anodes, which undergo the huge volume expansion/shrinkage upon the sodiation/desodiation processes, some types of polymer binders, such as the self-healing ones, can play a critical role in maintaining the structural integrity and electrochemical stability. Particularly, the chemical stability toward the solvent/active material and mechanical stability for the large volumetric changes should be the primary factors in achieving high-performance phosphorus anodes with a large reversible capacity and an oustanding cycle stability. Although there have been several previous studies that reported binders may have different effects on the electrochemical performances of phosphorus-based electrodes, the fundamental working mechanism of binder is yet hardly probed and poorly understood. Specifically, the basic impacts of binders on the physicochemical properties and electrochemical performances of phosphorus anodes have barely been explored in previous reports. At the same time, the understandings on the phase transformation and structure evolution of phosphorus anode materials have still been ambiguous.

Herein, we for the first time uncovered the physicochemical effects of traditionally used poly(vinylidene difluoride) (PVDF) binder and aqueous binders on the structural stabilities and electrochemical performances of P/C anodes through the synchrotron-based X-ray techniques. Unsurprisingly, the PVDF binder with a low flexibility and a poor coherence strength, which cannot accommodate the huge volume changes, was found to induce the severe oxidation of phosphorus in the preparation of P/C electrode. Besides, when it comes to the water-based binders, the major phase of phosphorus in electrodes can be retained, while the structural stability/integrity associated with electrochemical durability would be significantly improved. At the same time, the aqueous binders would strongly bond with P/C composites and carbon black together to the current collector, enabling the rapid migrations of electrons and ions. Nonetheless, it is unexpectedly revealed for the first time that the applications of certain binders would obviously determine the oxidation degrees of P/C electrodes, which greatly influenced their electrochemical properties. To elucidating and confirming the reaction mechanism of such surprising discovery, the phase transformation and evolution of phosphorus upon sodiation/desodiation were further clarified by the ex situ P K-edge X-ray absorption spectroscopies.

2. Results and Discussion

All the P/C electrodes, which are consisting of 70 wt% P/C active material, 15 wt% polymer binder, and 15 wt% conductive agent, are pasted onto copper foil as current collector. Seven commercial binders in total have been adopted in this study. According to different hydrophilic/hydrophobic properties for these binders with various molecular structures, the water and NMP (*N*-methyl pyrrolidone) have been respectively selected as solvents for aqueous binders (sodium alginate (SA), poly(acrylic acid) (PAA), sodium carboxymethyl cellulose (CMC), chitosan (CHI), polyethylene glycol (PEG), and polyvinylpyrrolidone (PVP)) and traditional poly(vinylidene difluoride) (PVDF) binder in the fabrication of electrodes. First, the impact of binders on the structural evolution of various P/C electrodes has been comprehensively studied in **Figures 1** and **2**.

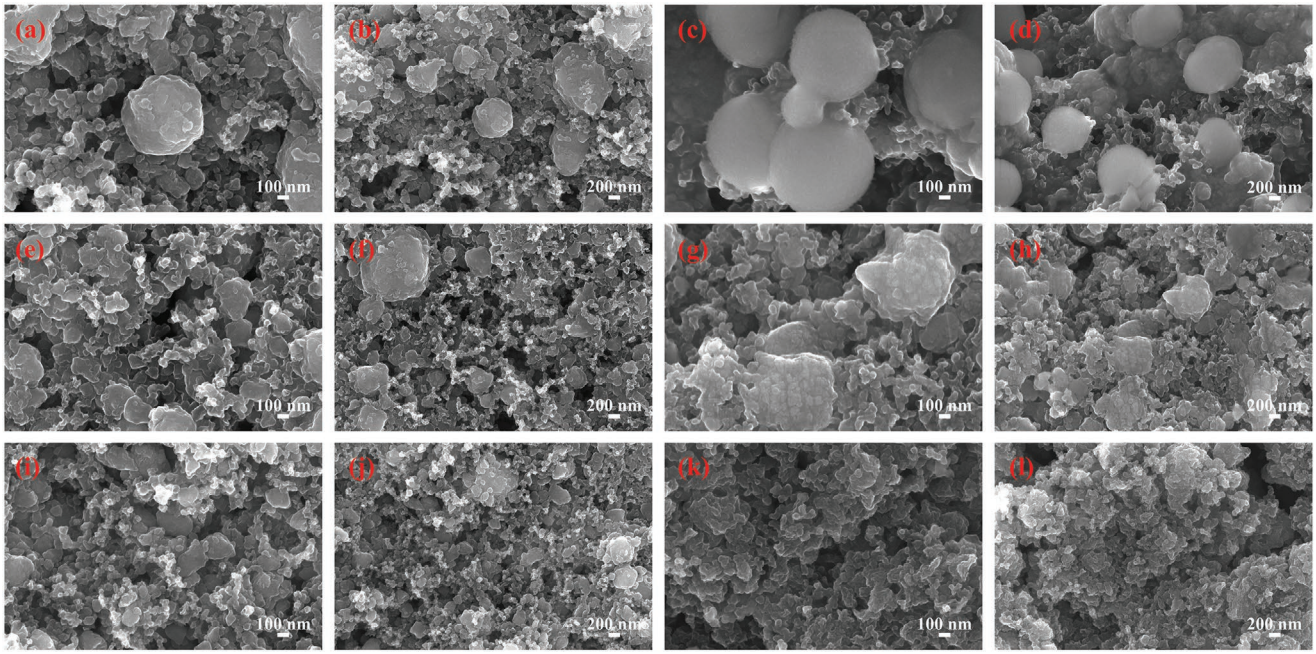

Figure 1. SEM images of the pristine a,b) SA, e,f) PAA, i,j) CMC and the cycled c,d) SA, g,h) PAA, k,l) CMC electrodes.

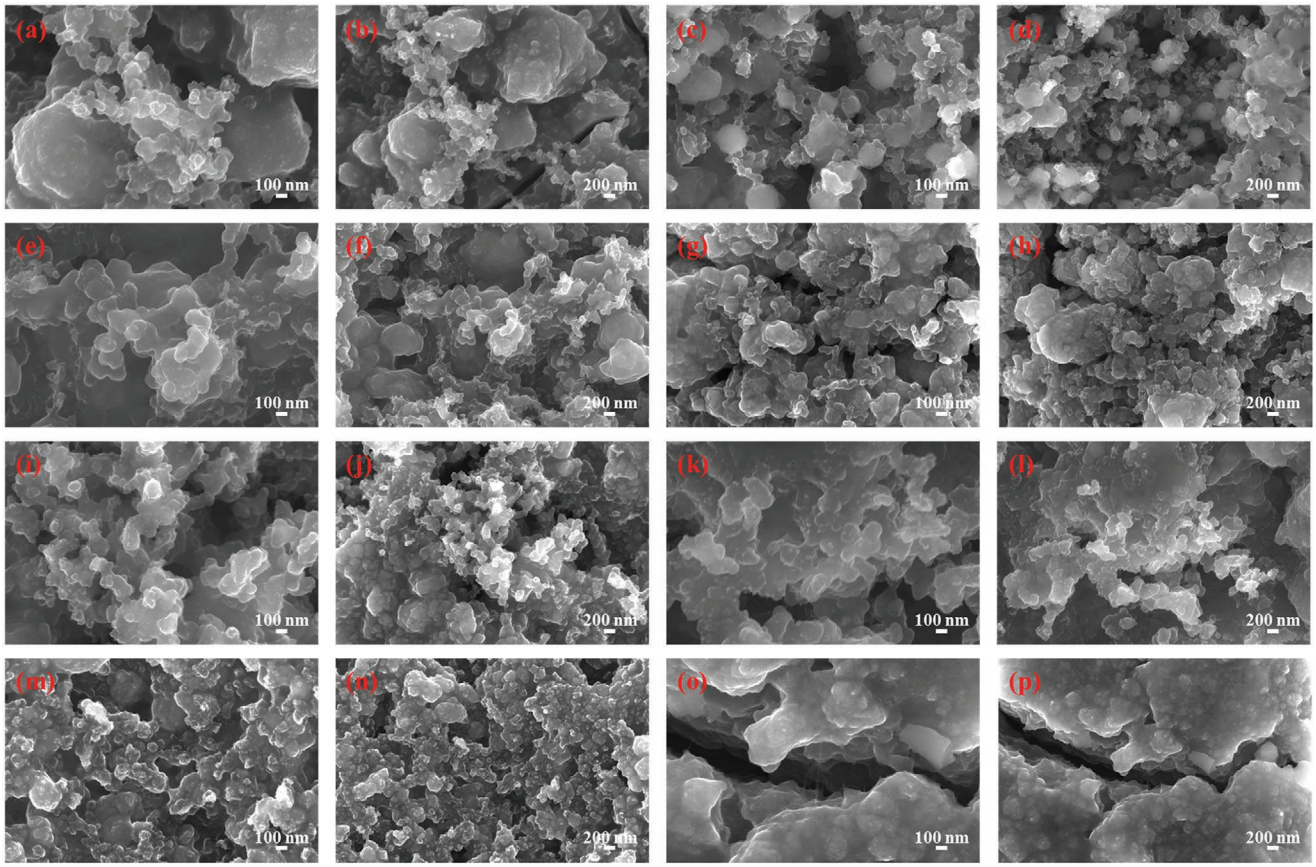

Figure 2. SEM images of the pristine a,b) CHI, e,f) PEG, i,j) PVP, m,n) PVDF and the cycled c,d) CHI, g,h) PEG, k,l) PVP, o,p) PVDF electrodes.

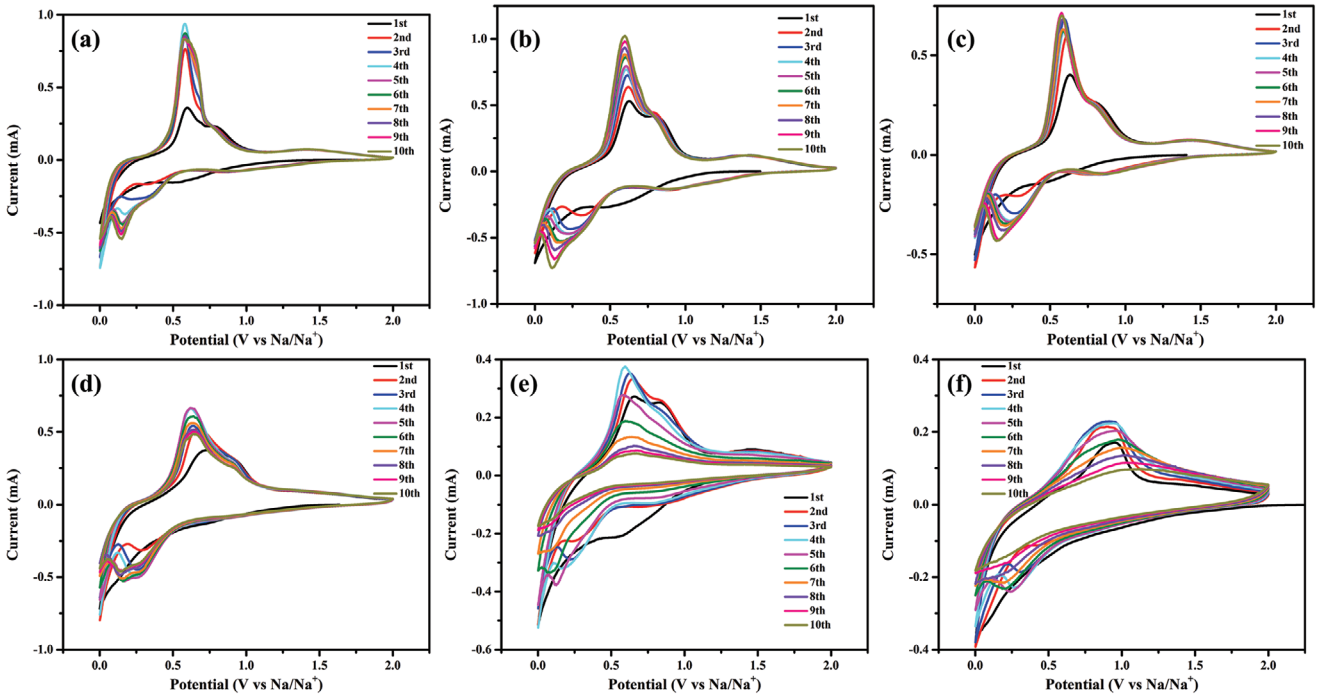

Figure 3. CV curves of a) SA, b) PAA, c) CHI, d) PEG, e) PVP, and f) PVDF electrodes at a scan rate of 0.2 mV s^{-1}.

As shown in Figure 1a,b for the SA electrodes, the small particles below 200 nm are uniformly distributed around the larger particles that are around 400–600 nm. Carbon black, with an average size of 100 nm, associated with some P/C nanoparticles, can be found between the large particles. Similarly, the PAA electrodes of Figure 1e,f and CMC electrodes of Figure 1i,j both present an even distribution of small particles (≈200 nm) and tiny carbon black particles (≈100 nm) around the larger particles (300–800 nm). Admittedly, a partial aggregation of tiny particles occurs in these electrodes, the mixtures of P/C composites and conductive agents are uniformly dispersed on the copper foils. Importantly, these mixtures are bonded together by the functional binders with hydroxyl groups. To understand the structural stabilities of electrodes using different binders, their morphologies were further characterized after 20 cycles of charging/discharging, as shown in Figure 1. Interestingly, the structures of large particles around 400–600 nm can be maintained, while the tiny carbon blacks around 100 nm are still located around the large particles for SA electrodes in Figure 1c,d. Even though several small particles around 200 nm, partially agglomerate to form the larger granules around 600 nm, most particles below 200 nm appear between the larger particles, for the PAA electrodes in Figure 1g,h. When it comes to the electrodes fabricated using CMC binder after cycling in Figure 1k,l, the small particles around 200 nm and tiny carbon black particles around 100 nm, retain their structures without severe aggregations.

Figure 2 further compares the morphological evolutions of the CHI, PEG, PVP, and PVDF electrodes upon cycling. For the pristine CHI electrode in Figure 2a,b, the small particles below 200 nm are situated between the larger particles around 1 µm. At the same time, the tiny particles of carbon black around 100 nm can be found surrounding the smaller particles around 200 nm and larger granules around 400 nm, as displayed in Figure 2e,f for the PEG electrode and Figure 2i,j for the PVP electrode. Additionally, most small particles below 200 nm become severely aggregated, generating the micron-sized bulk particles for PVDF electrode in Figure 2m,n. When it comes to the electrodes using CHI as a binder, several spherical particles around 300 nm near the tiny carbon black particles around 100 nm are evenly distributed in the gaps between the large agglomerated granules after 20 cycles, as shown in Figure 2c,d. The cycled PEG electrodes also present a uniform distribution of aggregated particles around 200 nm in Figure 2g,h. Furthermore, the aggregation of particles below 200 nm is more obvious for cycled PVP electrodes in Figure 2k,l. For the cycled PVDF electrodes, only thick bulks consisting of small particles below 200 nm, can be observed in Figure 2o,p. It is also clear that the broken PVDF chains occur between two large bulks, indicating the low structure stability of PVDF electrode. The improved structural stability of SA, PAA, and CMC electrodes with the minimal structural pulverizations, should be originated from the strong bonding capability of these binders to confine active materials and conductive agents, and their high structural flexibility to accommodate the large strains from the huge volume expansion/shrinkage during the repeated sodiation/desodiation processes.[22]

Subsequently, the electrochemical behaviors for electrodes made with different binders were compared using the cyclic voltammetry (CV) at a scan rate of 0.2 mV s^{-1} between 2.0 and 0.001 V (vs Na/Na^+). During the first discharging process, both the SA and PAA electrodes present a broad peak around 0.6 V, because of the irreversible electrolyte decomposition and formation of solid electrolyte interphase (SEI), as shown in **Figure 3**a,b. Similarly, this peak can also be found in the first sodiation of CMC electrode, as shown in Figure S4 (Supporting

Information). However, this feature becomes unclear for CHI, PEG, PVP, and PVDF electrodes, implying a failure in generating a robust SEI film which can effectively suppress the side reactions on the surface between the electrode and electrolyte. A sharp peak around 0.001 V is observed at the end of the first cathodic process for all electrodes. During the first charging process, three peaks at 0.58, 0.81, and 1.42 V can be observed in Figure 3a for the SA electrode, indicating a gradual phase conversion from Na_3P to Na_2P, NaP, and NaP_7 compounds, respectively.[9g,12m,23] Simultaneously, the position for the strongest anodic peak in Figure 3b of the PAA electrode moves to 0.59 V, while the first two peaks for the CMC electrode move to the lower positions of 0.55 and 0.79 V, respectively. In addition to the strongest peak at 0.58 V, the CHI electrode in Figure 3c displays two other features at 0.83 and 1.45 V, respectively. For the PEG electrode in Figure 3d, only two peaks at 0.63 and 0.93 V can be found in the first charging process. The PVP electrode in Figure 3e shows two strong peaks at 0.65 and 0.84 V with a broad peak at 1.48 V upon the initial charging process. When it comes to the PVDF electrode, only one peak at 0.94 V can be observed in the first anodic process. In the subsequent cycles, a noticeable cathodic peak for the SA electrode is located at 0.15 V, while the positions of this corresponding feature in the PAA, CMC, and CHI electrode, gradually move to the lower voltage regions, regardless of this common feature around 0.001 V. The PEG, PVP, and PVDF electrodes also present several strong cathodic peaks between 0.25 and 0.001 V. Due to the electrode activation in the first few cycles, the intensity of the first anodic peak around 0.6 V, gradually increases for SA, PAA, CMC, CHI, and PEG electrodes. However, the anodic peaks for PVP and PVDF electrodes subsequently move to the lower voltage positions, while the peak intensities continuously decrease upon cycling, hinting at a poor electrochemical activity/reversibility for PVP and PVDF electrodes. Importantly, the lower anodic peak positions and stable peak intensities for SA, PAA, and CMC electrodes, compared with the higher anodic peak positions and decreasing peak intensities for other electrodes, further demonstrate the structural and electrochemical merits in binder optimization for lowering the electrochemical polarization and extending the cycle durability.

In **Figure 4**, the galvanostatic discharge-charge tests were applied to investigate the electrochemical properties of electrodes using different binders at 400 mA g^{-1}. In the first cycle for Figure 4a, the SA electrode delivers a remarkable discharging capacity of 1984 mAh g^{-1} and a large charging capacity of 1734 mAh g^{-1} with a high columbic efficiency of 87.4%. The PAA and CMC electrodes in Figure 4b and Figure S5a (Supporting Information), display the first discharging capacities of 1379 and 1572 mAh g^{-1} as well as the reversible charging capacities of 1155 and 1374 mAh g^{-1}, along with the initial columbic efficiencies of 83.8% and 87.4%, respectively. The CHI electrode exhibits the initial discharging and charging capacities of 1326 and 957 mAh g^{-1} with an initial columbic efficiency of 72.2%, respectively. Unfortunately, the PEG and PVP electrodes present the initial discharging capacities of 867 and 569 mAh g^{-1} with the low columbic efficiencies of 56.1% and 70.0%, respectively. Surprisingly, the PVDF electrode could only obtain a discharging capacity of 604 mAh g^{-1} and a charging capacity of 276 mAh g^{-1} with a very poor columbic efficiency of 45.7%, which are much lower than the electrochemical results for the electrodes using aqueous binders. Table 2 further compared the charging capacities of different electrodes at a current density of 400 mA g^{-1}. Because the charging voltage

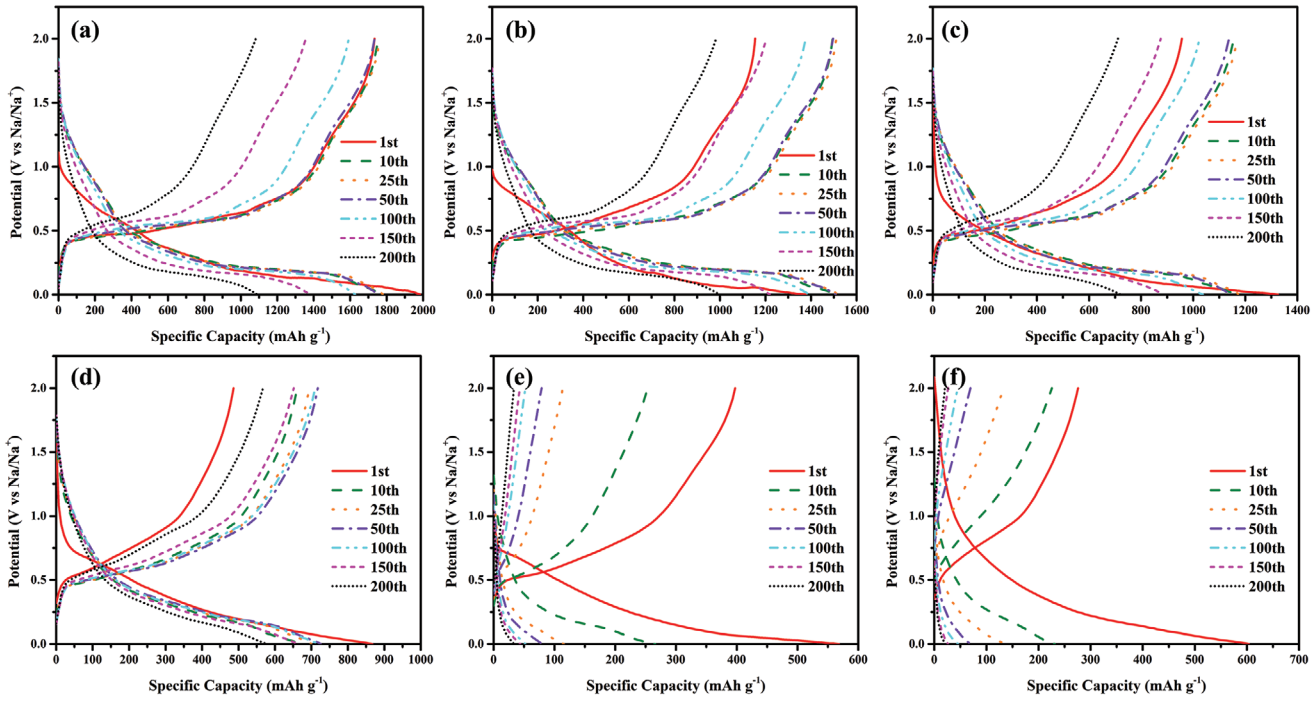

Figure 4. Discharging/charging profiles for a) SA, b) PAA, c) CHI, d) PEG, e) PVP, and f) PVDF electrodes at a current density of 400 mA g^{-1}.

plateau is a critical parameter for anode materials, this value gradually increased from 0.5 V for the SA, PAA, CMC, and CHI electrodes to 0.6 V for the PEG electrode and 0.75 V for the PVP and PVDF electrodes, which are consistent with the results in comparison of cathodic features in Figure 3. The decreased phosphorus utilization and fast capacity degradation for PEG, PVP and PVDF further question their capability in fabricating a stable and durable phosphorus electrode with a high electrochemical activity. Although the charging voltage plateau for SA, PAA and CMC electrodes gradually increases with cycling, it is straightforward to find the merits of these functional binders in promoting the electrochemical activity and reversibility by effectively bonding P/C composites with conductive agents on the current collectors.

To further understand the relationship between binder selections and electrochemical properties, the cycle performances were evaluated between 2.0 and 0.001 V (vs Na/Na^+) at the various current densities, as presented in **Figure 5**. Specifically, the specific capacity based on total weight of the P/C composite is shown on the left vertical axis, while the corresponding value at right vertical axis can be calculated based on the weight of P ignoring the capacity contribution from carbon black. When applied at a low current density of 100 mA g^{-1} for Figure 5a, the slow but progressive sodiation/desodiation reactions enable the SA, PAA, and CMC electrodes to have the large discharging capacities of 2174, 1954, and 1887 mAh g^{-1} as well as the highly reversible charging capacities of 1825, 1681, and 1683 mAh g^{-1} in the first cycle, respectively. At the same time, the CHI, PEG, and PVP electrodes display the initial discharging/charging capacities of 1729/1271, 1603/1064, and 1295/919 mAh g^{-1}, respectively. However, the electrode made using PVDF merely exhibits a low discharging capacity of 721 mAh g^{-1} and a poor charging capacity of 501 mAh g^{-1} at the beginning. In terms of the initial columbic efficiency in first cycle, SA, PAA, CMC, CHI, PEG, PVP, and PVDF present 84.0%, 86.0%, 89.2%, 73.5%, 66.4%, 71.0%, and 69.5%, respectively. After 50 cycles at 100 mA g^{-1}, SA, PAA, CMC, CHI, and PEG electrodes could demonstrate the reversible charging capacities of 1741, 1695, 1650, 1253, and 1019 mAh g^{-1} with the ultrahigh capacity retentions of 95.0%, 98.0%, 97.3%, 97.3%, and 95.7% starting from the 2nd cycle, respectively. But the PVP and PVDF electrodes could only deliver the charging capacities of 677 and 76 mAh g^{-1} with the relatively low capacity retentions of 73.9% and 17.0% after the 2nd cycle, respectively. When the current density was adjusted to 200 mA g^{-1}, the SA, PAA, CMC, CHI, and PEG electrodes possess the first discharging/charging capacities of 2061/1761, 1847/1574, 1849/1603, 1612/1215, and 1466/1011 mAh g^{-1} in Figure 5b, respectively. As compared in **Table 1**, the SA, PAA, CMC, CHI, and PEG electrodes could still have highly reversible charging capacities of 1561, 1450,

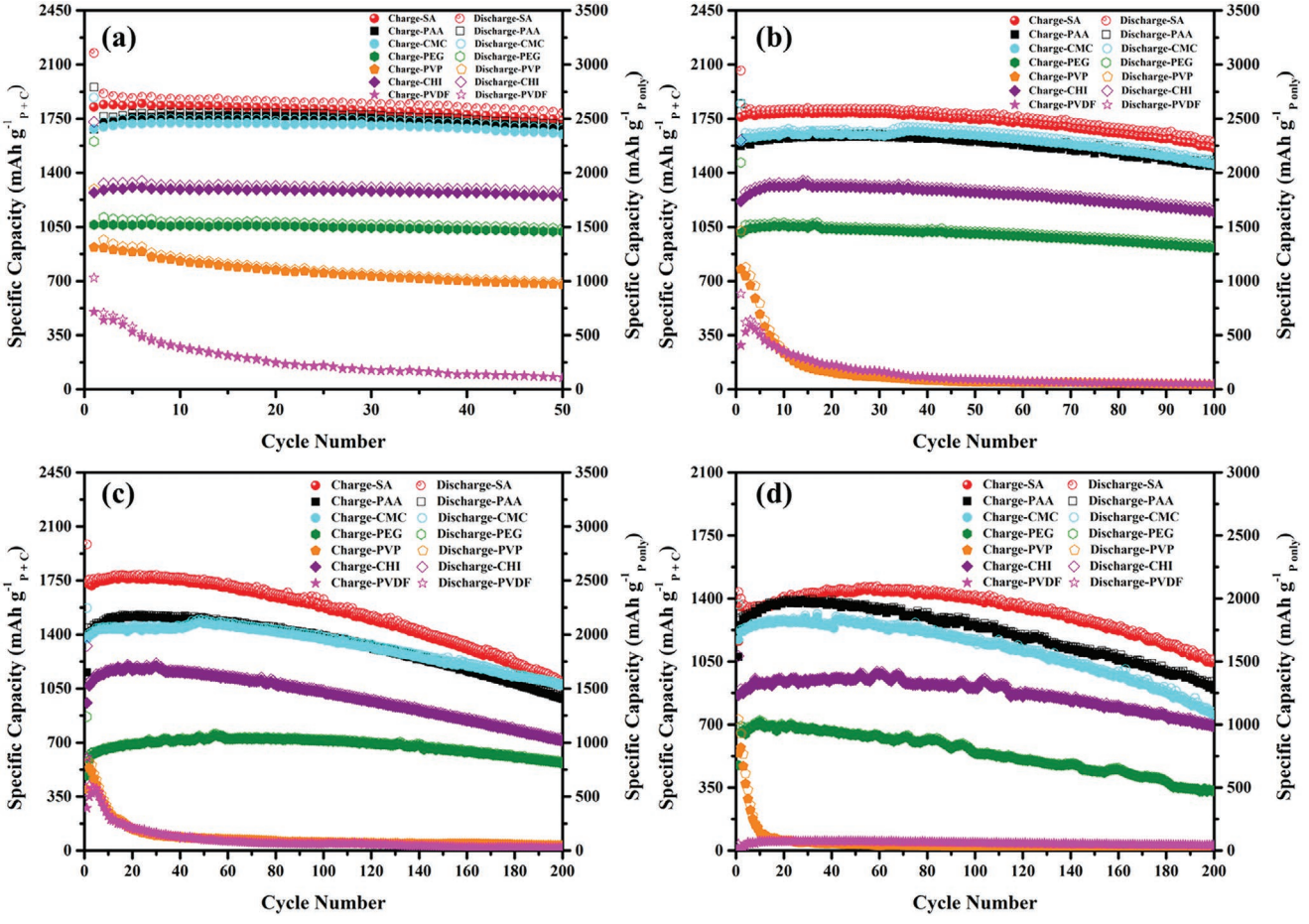

Figure 5. Cycle performances of different electrodes at the current densities of a) 100, b) 200, c) 400, and d) 800 mA g^{-1}.

Table 1. Comparison of charging capacities after different cycles for various electrodes at a current density of 200 mA g^{-1}.

Charging capacity [mAh g^{-1}]	1st	2nd	5th	10th	25th	50th	75th	100th
SA	1761	1774	1779	1785	1789	1748	1674	1561
PAA	1574	1592	1605	1627	1634	1609	1526	1450
CMC	1603	1624	1636	1654	1646	1643	1567	1455
CHI	1215	1243	1292	1311	1306	1272	1217	1145
PEG	1011	1029	1048	1060	1033	1006	967	914
PVP	778	734	487	233	87	48	41	30
PVDF	286	372	355	244	129	64	43	36

1455, 1145, and 914 mAh g^{-1} over 100 cycles with the considerable capacity retentions of 88.6%, 92.1%, 90.8%, 94.2%, and 90.4%, respectively. Although the PVP and PVDF separately display the initial discharging/charging capacities of 1026/778 and 618/286 mAh g^{-1}, the reversible capacities rapidly drop to 30 mAh g^{-1} upon cycling, hinting at the difficult electron/ion migrations because of using these binders.

Furthermore, the cycle performances for various electrodes using a current density of 400 mA g^{-1} were also compared and listed in Figure 5c and **Table 2**, respectively. After 200 cycles, the SA, PAA, CMC, CHI, and PEG electrodes display the capacity retentions of 62.8%, 69.5%, 76.9, 66.6%, and 96.6%, respectively. When cycling at 800 mA g^{-1} as shown in Figure 5d, the SA, PAA, and CMC electrodes can still deliver the initial discharging/charging capacities of 1436/1163, 1291/1077, and 1367/1171 mAh g^{-1}, while the CHI and PEG electrodes also present the initial discharging/charging capacities of 1081/862 and 682/475 mAh g^{-1}, respectively. After 200 cycles, the SA, PAA, CMC, CHI, and PEG electrodes could retain the discharging/charging capacities of 1064/1048, 902/893, 767/753, 696/690, and 335/330 mAh g^{-1} with the capacity retentions of 90.1%, 82.9%, 64.3%, 80.0%, and 69.5%, respectively. The charging capacities of different electrodes at a current density of 800 mA g^{-1} were compared in **Table 3**. Unfortunately, the cycle life for PVP and PVDF electrodes at 400 and 800 mA g^{-1} only last for 20 cycles. As compared in Tables S2 and S3 (Supporting Information), the P/C electrodes using SA, PAA, and CMC binders would demonstrate higher initial columbic efficiencies and charge capacity retention rates than these of anodes utilizing CHI, PEG, PVP, and PVDF binders. It is also noteworthy that the increase of reversible capacity for phosphorus electrodes at the beginning of the cycling should attributed to the activation of P/C composites during the sodiation/desodiation process.[24] Critically, the strikingly different electrochemical performances for various electrodes using diverse binders, further testified the structural and chemical significance of a suitable binder to fully utilizing active materials in an electronically/ionically conductive and highly stable structure.

The outstanding rate capabilities of SA and PAA electrodes were further confirmed in **Figure 6** and **Table 4**. The SA electrode is found to obtain the stable charging capacities of 1835, 1811, 1805, 1465, 1430, and 1203 mAh g^{-1} at a current density of 100, 200, 400, 800, 1600, and 3200 mA g^{-1}, respectively. At the same time, the PAA electrode delivers the reversible capacities of 1740, 1655, 1507, 1366, 1173, and 824 mAh g^{-1} at a current density of 100, 200, 400, 800, 1600, and 3200 mA g^{-1}, respectively. Increasing the current density to 4800 and 6400 mA g^{-1}, SA electrodes could still deliver the reversible capacities of 817 and 761 mAh g^{-1}, which are higher than those for PAA electrodes (449 and 256 mAh g^{-1}, respectively). Further increasing the current density to 8000 mA g^{-1}, the reversible capacities of 401 and 242 mAh g^{-1} could be achieved for SA and PAA electrodes, respectively. Interestingly, the highest reversible capacity of 1835 mAh g^{-1} for SA electrodes based on the total weight of P/C composite, corresponds to 2521 mAh g^{-1} based on weight of P (considering the specific capacity of carbon black is 100 mAh g^{-1} at 100 mA g^{-1}), which is approaching the theoretical specific capacity of 2596 mAh g^{-1} for red P. This result clearly proves the full utilization of active P in SA electrode with a highly stable structure. Particularly, a superior cycle performance of a 90.1% capacity retention over 200 cycles at 800 mA g^{-1} and an outstanding rate capability with 401 mAh g^{-1} at 8000 mA g^{-1} for the SA electrode are very competitive, compared with the electrochemical properties of P/C anodes in the similar systems.[9g,12a–c,f–h,k,l,p,ab,17,19,23] Based on the excellent cycle stability and rate capability, the SA electrode in Figure S6a

Table 2. Comparison of charging capacities after different cycles for various electrodes at a current density of 400 mA g^{-1}.

Charging capacity [mAh g^{-1}]	1st	2nd	5th	10th	25th	50th	100th	150th	200th
SA	1734	1724	1733	1753	1763	1733	1592	1356	1082
PAA	1155	1414	1461	1495	1510	1496	1377	1204	983
CMC	1374	1392	1427	1437	1442	1472	1369	1223	1071
CHI	957	1067	1128	1156	1170	1137	1025	876	717
PEG	487	587	633	661	695	718	710	652	567
PVP	398	536	428	254	113.8	79	52	43.1	33
PVDF	276	350	381	226	133	70	45	27	21

Table 3. Comparison of charging capacities after different cycles for various electrodes at a current density of 800 mA g^{-1}.

Charging capacity [mAh g^{-1}]	1st	2nd	5th	10th	25th	50th	100th	150th	200th
SA	1163	1355	1328	1350	1394	1437	1399	1257	1048
PAA	1077	1252	1300	1347	1382	1360	1255	1082	893
CMC	1171	1214	1234	1259	1267	1259	1160	1001	753
CHI	862	877	895	925	951	950	901	816	690
PEG	475	658	675	716	677	641	539	441	330
PVP	543	572	287	102	49	34	24	18	13
PVDF	12	15	38	49	53	53	46	38	32

(Supporting Information) could deliver the highly reversible capacities of 844, 789, 768, 627, and 437 mAh g^{-1} at 1600, 3200, 4800, 6400, and 8000 mA g^{-1} after 200 cycles, respectively. Additionally, the PAA in Figure S6b (Supporting Information) separately maintains the charging capacities of 788, 479, 340, 144, and 137 mAh g^{-1} at 1600, 3200, 4800, 6400, and 8000 mA g^{-1} after 200 cycles, while the CMC electrode barely works at a current density above 3200 mA g^{-1}.

According to the previous studies, the aqueous binders, including CMC[9f,g,12b,c,e,h,k,r,aa,14,16,21,23] and PAA,[12a,f,q,y,ab,18] were the primary choices for the early studies on the phosphorus anodes. Classically, the aqueous binders could effectively attach to the active materials and conductive agents via the abundant oxygen-containing functional groups, which is thus superior to PVDF binder merely combining the other components through the weak Vander Walls force from the hydrogen and fluorine

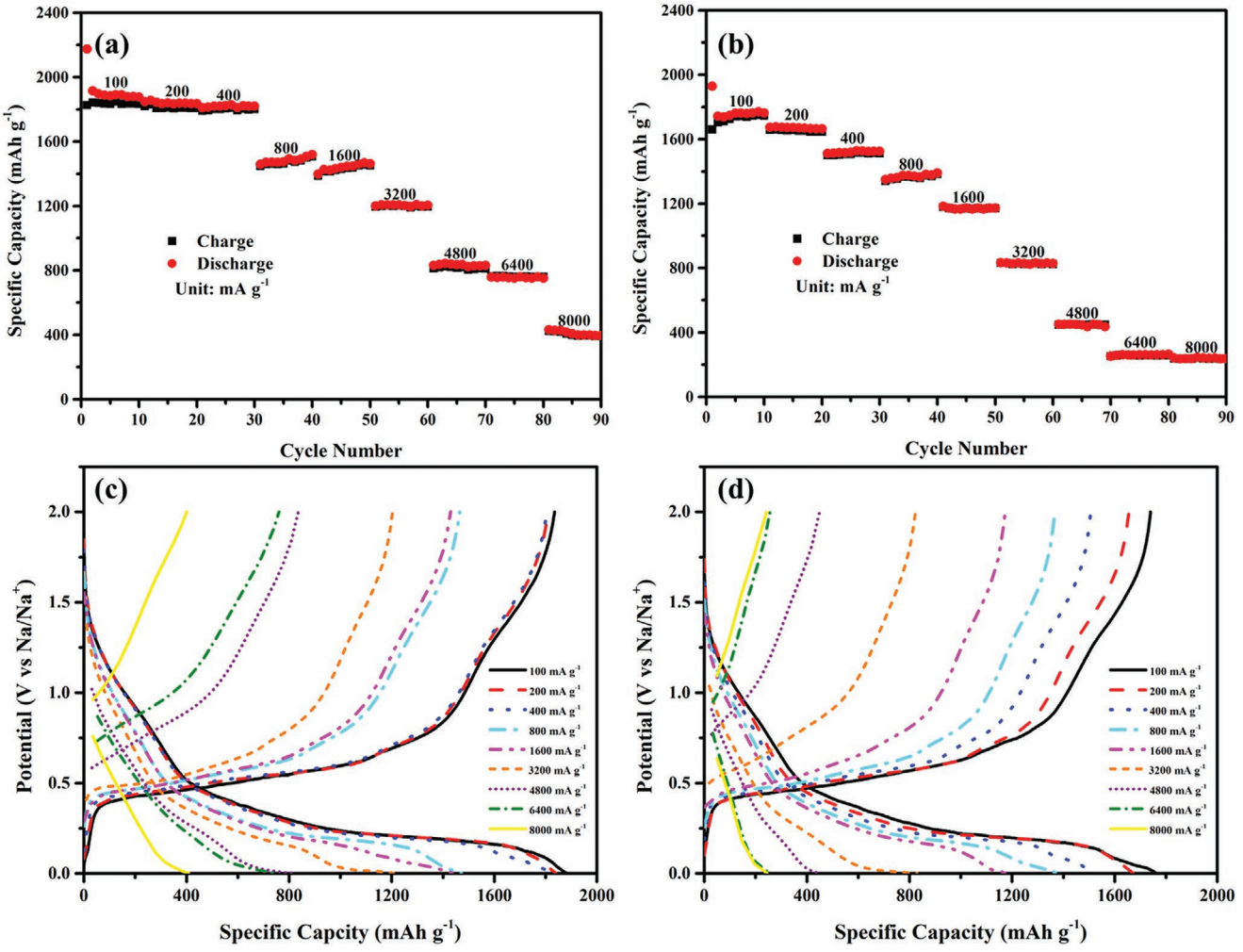

Figure 6. Rate performances for a) SA and b) PAA electrodes with the corresponding discharging and charging profiles for c) SA and d) PAA electrodes at the different current densities.

Table 4. Comparison of charging capacities for various electrodes at different current densities.

Current density [mA g^{-1}]	100	200	400	800	1600	3200	4800	6400	8000
SA [mAh g^{-1}]	1835	1811	1805	1465	1430	1203	817	761	401
PAA [mAh g^{-1}]	1740	1655	1507	1366	1173	824	449	256	242
CMC [mAh g^{-1}]	1719	1647	1490	1264	871	479	No performance		

atoms.[22] A prevailing question on the PVDF binder, should be its rigid structure with a low flexibility and a poor adhesive capability, which cannot tolerate the enormous mechanical strains imparted by the huge volume changes occurring the multi-electron reactions for the high-capacity anode materials.[12x,25] Without the strong chemical bonding between electrode components, the structural collapse and electrode pulverization induce the loss of an electrical contact between the active material and current collector, leading to a rapid capacity decay and a battery failure. However, there are yet lack of effective proofs to show in addition to the structural considerations, whether there is the phase evolution of active material (phosphorus) in the fabrication of electrode.

Importantly, the synchrotron-based X-ray techniques, which have been known for their uniquely elemental sensitivity in detecting the extremely slight changes to chemical states, were further employed to characterize various P/C electrodes with different binders. The tunable photon energy, ranging from several hundred electronvolt (eV) for soft-X-rays to a few hundred thousand eV for hard X-rays, offers a spectroscopic opportunity to study the phase evolution from the surface to bulk.[26] **Figure 7**a presents the P K-edge X-ray absorption spectroscopies for different electrodes. The first peak at 2144.5 eV reflects the electron transition from the 1s core level to the vacant t2*(p-like) anti-bonding orbitals, and another two peaks at 2152.5 and 2168.9 eV may be related to the shape resonance (multiple scattering).[27] Specifically, the K-edge peak at 2144.5 eV corresponds to the P—P bonding, while the peak at 2152.5 eV and the broad peak at 2168.9 eV represent the P—O bonding in the species of $(PO_2)^{3-}$ and $(PO_4)^{3-}$, respectively.[12aa,25b,27,28] Comparing the X-ray absorption spectroscopies for different electrodes, the peak intensity for P—P bonding gradually decreases from the SA, PAA, and CMC to CHI, PEG, PVP, and PVDF electrodes. Simultaneously, the SA, PAA, and CMC electrodes only display a minor peak at 2152.5 eV for P—O bonding, while several stronger peaks emerge at the same position with the increasing intensities for the CHI to PVP, PEG, and PVDF electrodes. Additionally, a broad peak appeared at 2168.9 eV for the P—O bonding also increases in the intensity along with the peak at 2152.5 eV. The regular changes of the peaks for the P–P bonding and P–O bonding reveal the oxidation of phosphorus in electrodes utilizing the specific binders. As the preparation of electrodes follows the same procedure, the oxidation of phosphorus in P/C composite is proposed to happen during the fabrication process. Critically, the degree of oxidation slowly increases in the following order of the CHI, PEG, PVP, and PVDF electrodes, while the SA, PAA, and CMC electrodes demonstrate the negligible oxidation. To further clarify the oxidation effect for electrodes made using various binders, the synchrotron-based X-rays with the tunable penetration depths, are employed to collect the high-resolution P 2p X-ray photoelectron spectroscopies from the surface to bulk, as displayed in Figure 7b–d. Generally, the peak at 130.2 eV represents the unresolved P $2p_{3/2,1/2}$ feature while the peak around 134.0 eV shows the P—O bonding in the species of $(PO_2)^{3-}$ and $(PO_4)^{3-}$.[12aa,23,25b,28–30] Increasing the photon energy to 3000 eV, as shown in Figure 7b, the peaks for the P—P bonding weaken from the SA to PAA and CMC electrodes, while no such peak can be observed for the CHI, PEG, PVP, and PVDF electrodes. Additionally, the peaks for the P–O bonding at 134.0 eV increase from the SA to PAA, CMC, CHI, PEG, PVP, and PVDF electrodes. This situation clearly demonstrates the weak oxidation behaviors of the SA, PAA and CMC electrodes and severe oxidation phenomena imparted by the CHI, PEG, PVP and PVDF binders. Further increasing the photon energy to 4900 eV, the peaks for the P 2p feature move to 130.4 eV. The appearance of this peak in the SA, PAA, and CMC electrodes with the decreasing intensities are accompanied with its absence in the CHI, PEG, PVP, and PVDF electrodes. At the same time, the peaks at 134.0 eV for the P–O bonding have the increasing intensities in the order of the SA, PAA, CMC, CHI, PEG, PVP, and PVDF. Even the photon energy is increased to 7000 eV (most bulk sensitive), the peak at 130.2 eV for the P–P bonding still did not appear for the CHI, PEG, PVP, and PVDF electrodes, while the changing rule of the peaks intensities in the high energy region (134.0 eV) for the P–O bonding is also the same as before, proving the orderly increasing oxidation degrees from the SA to PAA, CMC, CHI, PEG, PVP, and PVDF electrodes. This oxidation phenomenon and tendency, as identified by the high-resolution X-ray photoelectron spectroscopies, conform to the preliminary results from the X-ray absorption spectroscopies. To conclude, the selection of a suitable binder not only determines the structural stability of phosphorus anodes with the huge volume expansion/shrinkage, but also affects the phase purity of active phosphorus material in the fabrication of the electrodes. Additionally, the applications of various binders in P/C electrodes are supposed to determine the structures, compositions, and morphologies of SEI films after cycling. Particularly, the formation of SEI layer would be more easier to proceed on the fresh surfaces of P/C electrodes with relatively low oxidation degrees using SA, PAA, and CMC binders than that of anodes applying CHI, PEG, and PVP binders. However, a robust and stable SEI film can hardly be produced on the highly oxidized P/C anode utilizing PVDF binder with a lowest active phosphorus, leading to a poor reversible capacity and a fast capacity degradation. With the assistance of ionically conductive and electrically insulating SEI films, which can prevent the structural collapse of large-capacity electrodes upon cycling and suppress their side reactions with reactive electrolytes, the P/C anodes using SA, PAA, and CMC binders would deliver higher reversible capacities and better cycle performances than that of anodes applying CHI,

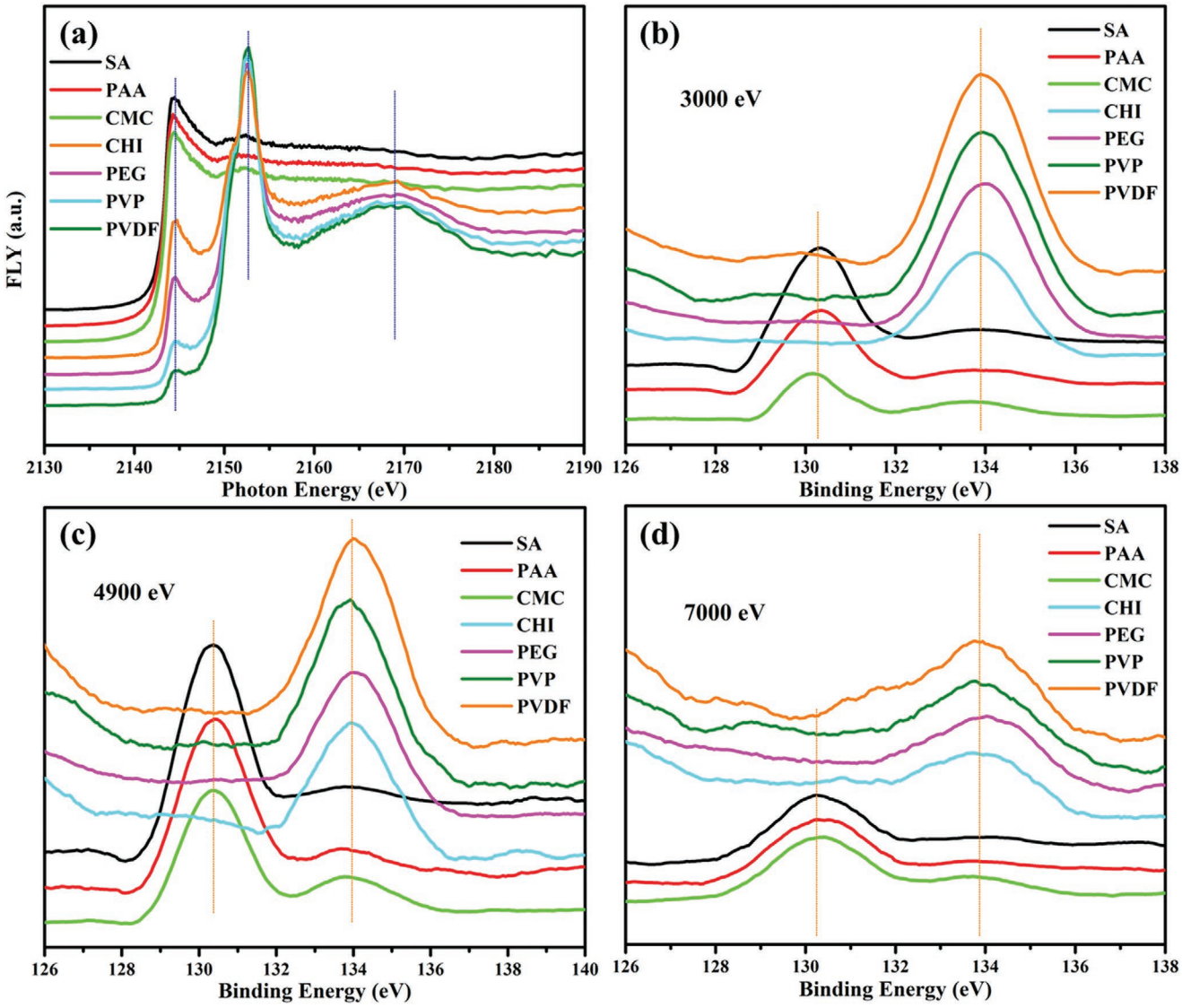

Figure 7. a) Synchrotron-based P K-edge X-ray absorption spectroscopies and b–d) depth-oriented P 2p X-ray photoelectron spectroscopies with variable photon energies for different electrodes.

PEG, and PVP binders. At the same time, the accumulation of insulating phosphate layers on the surface of P/C anodes would severely impede the ionic/electronic migrations across the electrolyte/electrode interface, further deteriorating the rate capabilities of highly oxidized electrodes.

To understand the phase transformations and reaction mechanisms of phosphorus anodes, the highly sensitive ex situ P K-edge X-ray absorption spectroscopies were conducted for different electrodes in **Figure 8**. Because the penetration depth of X-rays with a medium energy (≈2000 eV) is usually below 10 nm, this ex situ detection presumably provides the detailed information toward SEI formation and phase evolution of P/C composites made with different binders during the sodiation/desodiation processes.

For SA electrodes, as shown in Figure 8a, only a major peak within the A region of 2144.5 eV can be observed for pristine electrode, while the intensity for peak in the D region of 2152.5 eV has been weakened by the mylar film with a thickness of 4 µm, which is employed to prevent the physical contact between sample and air. After discharging to 0.5 V, the SA electrode displays a peak at a higher energy position of 2144.8 eV and a broad peak at the C region of 2150.5 eV, while the intensity for peak in the D region of 2152.5 eV gradually increases. As the A position peak for the P–P bonding in the pristine material is related to the electron transition from the 1s core level to the vacant t2*(p-like) anti-bonding orbitals, while the peak in the C region represents the P–O bonding in P 1s-3p transition with depleted 3p charge from the $(PO_2)^{3-}$ species in Na_2HPO_2 or monovalent phosphorus inorganic/organic compounds.[27,28,30] Additionally, a broad peak in the D region is attributed to the P—O bonding from the $(PO_4)^{3-}$ species in $Na_xH_y(PO_4)_z$.[12aa,25b,27,28] Compared with the $(PO_4)^{3-}$ species on the surface which are products of the reactions between phosphorus and electrolyte, most $(PO_2)^{3-}$ species in the SEI film are normally resulted from the reactions between

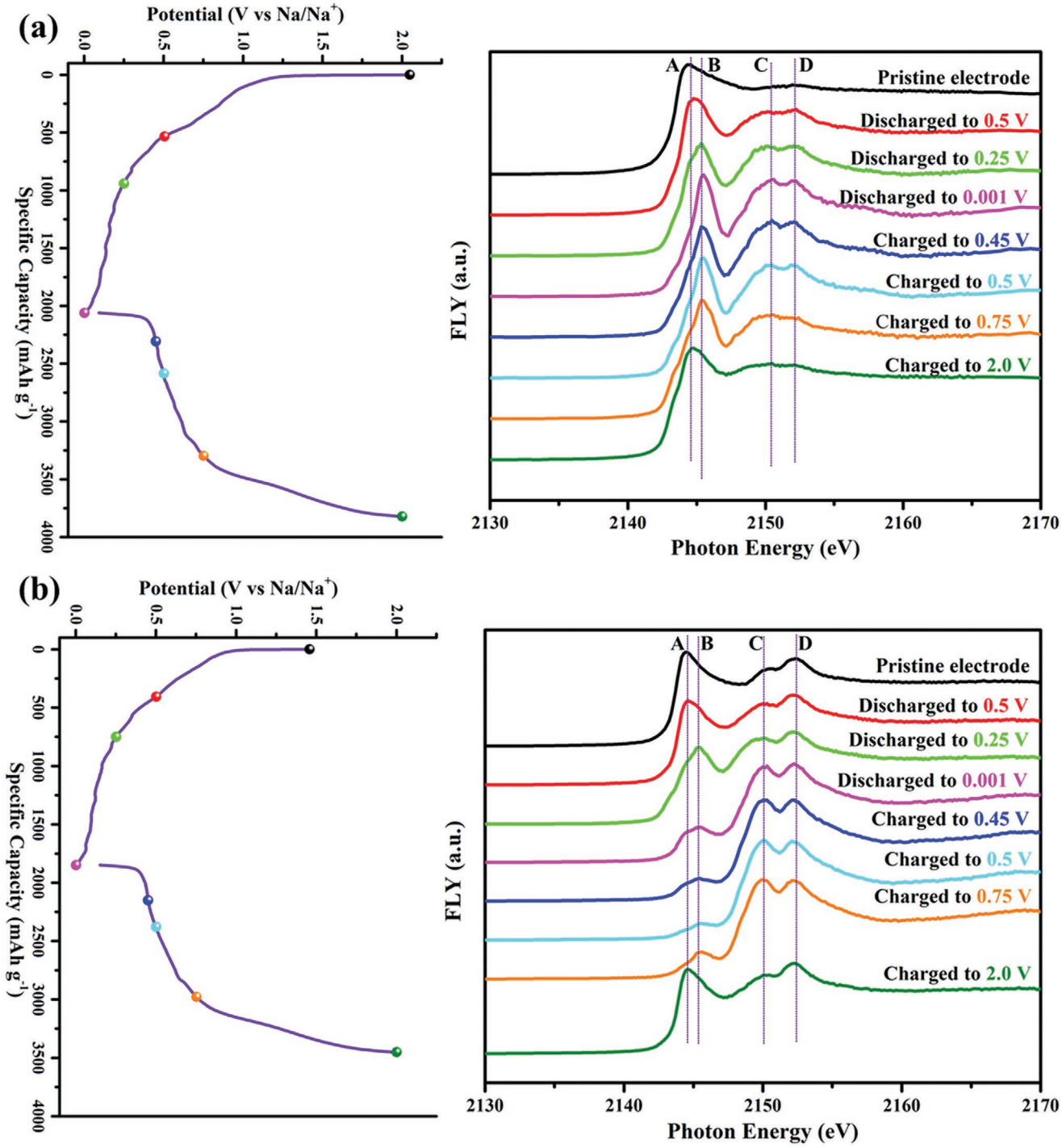

Figure 8. Ex situ P K-edge X-ray absorption spectroscopies (in right position) for a) SA and b) CMC electrodes at different states (in left position) during the discharging/charging processes. A region: The P—P bonding from the pristine P/C composite; B region: The P—Na bonding from the Na_xP; C region: The P—O bonding from the $(PO_2)^{3-}$ species; D region: The P—O bonding from the $(PO_4)^{3-}$ species.

the highly active sodiated phosphorus (Na_xP) compounds, the $(PO_4)^{3-}$ species, the residual phosphorus, and the electrolyte.[28a] When discharging to 0.25 V for the SA electrode, a new peak emerges at the B position of 2145.5 eV, which could be assigned to the P–Na bonding in the formation of Na_xP. At the same time, the peaks in the C and D regions have not changed in shape and intensity. Interestingly, the SA electrode discharged to 0.001 V shows a sharp peak in the B region of 2145.5 eV, indicating the stronger bonding between the P and Na atoms. Simultaneously, the peak at the C region become more obvious, as a result of the increasing side reactions between Na_3P and electrolyte. Subsequently, the peak within the B region presents no difference

after charging the SA electrode to 0.45, 0.5, and 0.75 V, while the peak in the C region gradually diminishes, hinting the instability of $(PO_2)^{3-}$ species during the charging process. The decrease of the peak intensity at the D position, for $(PO_4)^{3-}$ species in the SEI film, is related to their reactions with Na_xP to produce the unstable $(PO_2)^{3-}$ species. After charging back to 2.0 V, a major peak is found again at 2144.8 eV, while the peaks in the C and D regions completely disappeared, in accordance with the decomposition and dissolution of surface species.

Ex situ spectroscopic measurements of CMC electrodes are displayed in Figure 8b. Even though the same bonding features are presented in the spectroscopies, several differences on the phase evolution can be observed between the CMC and SA electrodes. As the pristine CMC electrode become partially oxidized, a minor peak at the C position around 2150.0 eV may be related to the P–O bonding in the $(PO_2)^{3-}$ species. At the same time, a broad peak in the D region at 2152.5 eV should be attributed to the P–O bonding in the $(PO_4)^{3-}$ species, while the major peak in the A region of 2144.5 eV represents the P features.[12aa,25b,27,28] Similarly, the peak within the A region does not change, while peaks in the C and D regions become more apparent for CMC discharged to 0.5 V. Notably, the movement of the first peak from 2144.5 to 2145.5 eV, further confirms the emergence of Na_xP in the CMC electrode discharged to 0.25 V. However, the peak intensity within the B region greatly decreases, while two broad peaks in the C and D regions become sharper with the increasing intensities, after discharging from 0.25 to 0.001 V for the CMC electrode. This phenomenon should be attributed to the considerable formation of the $(PO_2)^{3-}$ species via the complex reactions of Na_xP compounds and $(PO_4)^{3-}$ species with residual phosphorus and reactive electrolyte, while the increase of $(PO_4)^{3-}$ species may be originated from the severe reactions between phosphorus and electrolyte.[28a] Additionally, the increasingly accumulated $(PO_2)^{3-}$ species further hint at an obvious growth of SEI layer upon discharging to 0.001 V, which might attenuate the detecting signal for sodiated phosphorus compounds below the surface of active phosphorus. During the charging process from 0.001 to 0.75 V, the peak at the B position represents the existence of Na_xP with a little change, while the peaks in the C and D regions maintain their intensities. After charging back to 2.0 V for the CMC electrode, the first peak moves back to region A with a peak appearing at 2144.5 eV, while the peaks in the C and D regions return to their original locations, demonstrating the chemical instability of these surface species.

Based on the collected ex situ data, both SA and CMC present a good electrochemical reversibility with the formation and decomposition of the $(PO_2)^{3-}$ and $(PO_4)^{3-}$ species on the surface during the sodiation/desodiation processes. Importantly, the phosphate compounds, resulting from the oxidation of active phosphorus in the fabrication of electrodes, engage in the reactions between the electrolyte and pristine phosphorus as well as the sodiated phosphorus, further contributing to the emergence of SEI and evolution of microstructure for phosphorus anode upon the cycling. These synchrotron-based characterizations on the phase transformation and SEI formation of P/C composite would not only deepen the fundamental understanding on the reaction mechanisms for phosphorus anode materials, but also cast a light on the critical role of interface between active phosphorus and reactive electrolyte in morphological evolution.

Even though the primary choices of binder for P/C anode materials are aqueous binders, including CMC[9f,g,12b,c,e,h,k,r,aa,14,16,21,23] and PAA,[12a,f,q,y,ab,18] many researchers have reported the successful utilizations of PVDF binder in P/C anodes.[12l–n,19,20] Currently, the mechanical-milling method and vaporization-condensation approach are two major routes in the preparation of P/C anode materials. Importantly, the mechanical-milling method could remarkably downsize the pristine red phosphorus from microsized bulks into nanosized particles and completely mix it with conductive/flexible carbon materials. However, the P/C composites as synthesized via mechanical-milling route would possess large surface areas, rich surface defects, and high surface activation energies, which are quite favorable for their side reactions with oxygen in ambient air and solvent in electrode fabrication. Hence, we have surprisingly observed the unique function of binder in the fabrication of P/C electrode. Different from the mechanical-milling method, the vaporization-condensation approach could facilitate the confinement of phosphorus particles into highly stable mesoporous/microporous carbon matrixes, which could not only buffer the huge volume change and enable fast ionic/electronic migrations for phosphorus anode materials, but also suppress their parasitic reactions with oxygen in ambient air and solvent in electrode fabrication through limited contact areas.[12l–n,19,20] Therefore, the previously reported P/C composites obtained by vaporization-condensation route can still take advantage of PVDF binder in the preparation of electrode without sacrificing active phosphorus and reversible capacity.

The structural evolutions of electrodes prepared using different binders are illustrated in **Figure 9**. After the preparation of electrodes, the SA, PAA, and CMC electrodes display a minimal oxidation, while the CHI and PEG electrodes are partially oxidized. Furthermore, the PVP and PVDF electrodes were found to be severely oxidized in the bulk with the least amount of active red P. For the unoxidized electrodes, the highly flexible binders with a strong cohesive strength, can accommodate the huge volume change for the phosphorus anodes, and maintain the structural integrity during the sodiation/desodiation processes. When it comes to the partially oxidized electrodes, the oxidation layers on the surface can effectively buffer the large volume expansion/shrinkage during the discharging/charging processes. However, these aqueous binders with a low adhesive force, have a difficulty in withstanding these large volume changes, resulting in the isolation of particles and loss of electrical contact for active material to other components including the current collector. In the deeply oxidized electrodes, after cycling, the individual particles aggregate to form the large island-like particles, leading to the severe fracture of binders with a rigid structure and a poor flexibility. Even though the minor parts of the oxidation could help to cushion the volume expansion of the limited red P, the most insular bulks lost the electrical contact with the current collectors, inducing the extremely inferior electrochemical properties.

As the preparation of electrodes follows a similar procedure, the oxidation of electrodes may be attributed to the interactions between the binders and P/C composite in the solvent during the drying process. On the one hand, the NMP solution may react with the highly reactive P/C composites, leading to the severe oxidation of P/C electrode using PVDF

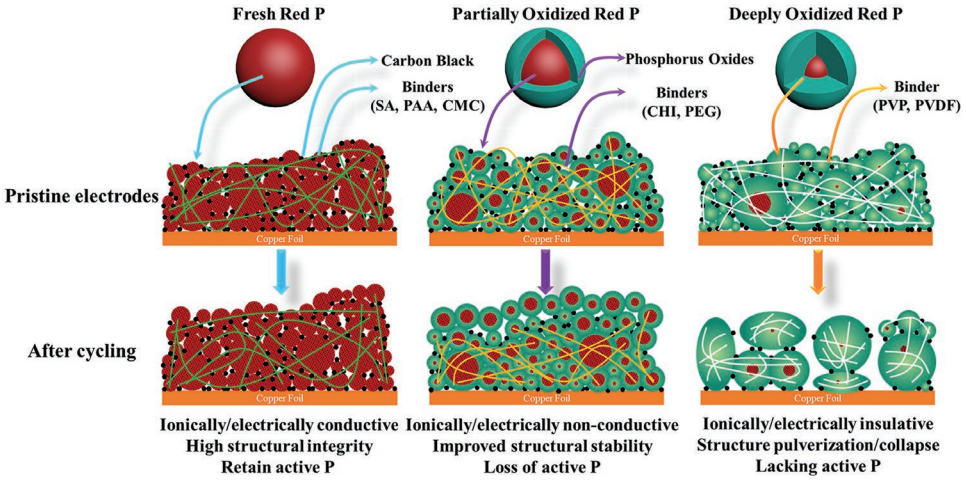

Figure 9. Schematic diagram of structural evolutions for electrodes using different binders.

binder. As characterized by P K-edge XAS in Figure S7 (Supporting Information), the highly reactive P/C composite would proceed a mild reaction with water and a noticeable oxidation in NMP, further hinting at the chemical complexity of reactions between P/C composite, solvents, and binders in the fabrication of electrode. On the other hand, a certain binder in the NMP may extend the evaporation time in an oven, resulting in an advanced oxidation of the electrode. Generally, the drying of 0.1 g P/C composite in 1 mL water at 60 °C under vacuum only takes less than 6 h, while the same process in 1 mL NMP would last for more than 12 h. Even though these speculations need to be further experimentally confirmed, it is still desirable to adjust the drying time at a lower temperature.

3. Conclusion

In summary, the relationship between different binders and their electrochemical properties for P/C composite was systematically investigated. Compared with the P/C anodes applying conventional PVDF binder, the electrodes utilizing aqueous binders have shown significantly improved electrochemical properties. For example, P/C using sodium alginate as the binder, delivered a highest reversible capacity of 1835 mAh g^{-1} and a superior rate capability of 401 mAh g^{-1} at 8000 mA g^{-1} as well as an outstanding cycle stability at 400 and 800 mA g^{-1} over 200 cycles. Surprisingly, the spectroscopic insights via the synchrotron-based X-ray techniques have offered a novel explanation regarding that the oxidation of active phosphorus in P/C composites is the key factor to determine their electrochemical properties, which has never been revealed in previous studies. The electrodes applying SA, CMC, and PAA, demonstrated the increased reversible capacities and enhanced electrochemical stabilities as well as improved rate capabilities. The benefits of these binders stem from a minimum oxidation of active phosphorus in electrodes and a high adhesive strength/flexibility to accommodate the huge volume changes upon cycling. Additionally, the electrodes with the poor electrochemical performances displayed an increased aggregation of the individual particles along with the high degree of surface oxidation for active phosphorus. Intriguingly, the ex situ P K-edge X-ray absorption spectroscopies for the electrodes using sodium alginate and sodium carboxymethyl cellulose as binders, demonstrated the formation and decomposition of monovalent phosphorus and phosphate intermediates during the sodiation and desodiation processes, due to the complicated interfacial reactions between active phosphorus and reactive electrolyte. The dramatic understandings on the structural evolution and phase transformation for phosphorus would undoubtedly facilitate the development of high-performance anode materials and further pave a new way to achieve highly durable, affordable, and sustainable SIBs with acceptable energy densities.

4. Experimental Section

Material Synthesis: The P/C composites were fabricated using a conventional ball-milling method at 600 rpm for 24 h. The weight ratio of red phosphorus (purity >97%, Sigma-Aldrich) and carbon black (Ketjen black, EC600JD) was adjusted to 7:3, according to the previous reports.[9g,12a] To fully mix phosphorus and carbon, the weight ratio of the iron steel milling balls, composed of three balls with different diameters (3, 5, and 8 mm) and same weight, to the whole starting materials was 20:1. All components, including the pristine materials and milling balls, were mixed in a steel jar and sealed in an Ar-filled glove box.

Electrochemical Measurements: In the preparation of electrodes, a slurry was obtained by homogeneously dissolving and mixing 70 wt% active materials (P/C composite), 15 wt% conductive agents (acetylene black), and 15 wt% polymer binders in a certain amount of the corresponding solvent, and then casted onto a copper foil. Specially, the electrodes using a traditional poly(vinylidene difluoride) (PVDF, Alfa Aesar) binder with *N*-methyl pyrrolidone (NMP, Sigma-Aldrich) as a solvent, aqueous binders of sodium alginate (SA, MP Biomedicals), sodium carboxymethyl cellulose (Na-CMC, Low viscosity, EMD Milipore), poly(acrylic acid) (PAA, ≈100 000, Sigma-Aldrich), polyvinylpyrrolidone (PVP, ≈1 300 000, Sigma-Aldrich), polyethylene glycol (PEG, 2000, Alfa Aesar) and chitosan (CHI, low molecular weight, Sigma-Aldrich) with water as a solvent, denoted as PVDF, SA, CMC, PAA, PVP, PEG, and CHI electrodes, respectively. After drying at 60 °C under vacuum overnight, the as-prepared electrodes were punched into ½ in. pellets and then pressed, yielding a loading weight

of ≈1.5 mg cm^{-2}. Considering the interfacial instability of phosphorus anode in ambient air, all as-prepared phosphorus electrodes should be immediately transferred into an Ar-filled glove box after drying process to suppress the potential surface oxidation of active phosphorus.[24] The 2032-type coin cells, consisting of phosphorus electrode as a cathode, polypropylene membrane (Celgard 3501) as a separator, sodium metal as an anode in the electrolyte, were employed to study the electrochemical performances of the phosphorus electrodes using different binders. The electrolyte was 1.0 mol L^{-1} sodium perchlorate in a solution of ethylene carbonate (EC) and diethyl carbonate (DEC) (1:1 in volume) with the 10 wt% addition of fluorinated ethylene carbonate (FEC). The cyclic voltammetry (CV) at a sweep rate of 0.2 mV s^{-1} was conducted by a Biologic VMP3 electrochemical station and the electrochemical discharging/charging performance was measured by a LAND (Wuhan Kingnuo Electronics, China) cycler between 0.001–2.0 V (vs Na/Na^+) at the various current densities under room temperature.

Physical Characterizations: Morphological evolutions of electrodes after the discharging/charging processes were observed by a Hitachi S-4800 field emission scanning electron microscope (FE-SEM) operated at 5 keV. For the synchrotron-based X-ray techniques, the P K-edge X-ray absorption spectroscopy (XAS) in fluorescence yield (FLY) was collected in the Soft X-ray Microcharacterization Beamline (SXRMB) at Canadian Light Source (CLS) to understand the structural information of electrodes with different binders and further track the phase transformation of phosphorus electrodes upon the sodiation/desodiation. Additionally, the depth-oriented high-energy X-ray photoelectron spectroscopy (XPS) measurements with a pass energy of 200 eV and three different photon energies of 3000, 4900, and 7000 eV were performed at the same beamline to study the effects of surface passivation on the electrochemical properties.[31]

Supporting Information

Supporting Information is available from the Wiley Online Library or from the author.

Acknowledgements

This research was supported by the Natural Science and Engineering Research Council of Canada (NSERC), the Canada Research Chair Program (CRC), the Canada Foundation for Innovation (CFI), and the University of Western Ontario (UWO). W.X. thanks to the financial support from China Postdoctoral Science Foundation (2019M653705). The synchrotron work was performed at the CLS, a national research facility of the University of Saskatchewan, which is supported by CFI,NSERC, the National Research Council (NRC), the Canadian Institutes of Health Research (CIHR), the Government of Saskatchewan, and the University of Saskatchewan. The technical assistance of SXRMB staff, Dr. Qunfeng Xiao and Dr. Yongfeng Hu, is gratefully acknowledged.

Conflict of Interest

The authors declare no conflict of interest.

Keywords

binder, phosphorus/carbon anode, sodium alginate, sodium-ion batteries, surface oxidation

Received: January 3, 2020
Revised: April 9, 2020
Published online:

[1] a) J. M. Tarascon, *Nat. Chem.* **2010**, *2*, 510; b) B. Dunn, H. Kamath, J. M. Tarascon, *Science* **2011**, *334*, 928; c) J.-M. Tarascon, M. Armand, *Nature* **2001**, *6861*, 359.

[2] a) V. Palomares, P. Serras, I. Villaluenga, K. B. Hueso, J. Carretero-González, T. Rojo, *Energy Environ. Sci.* **2012**, *5*, 5884; b) H. Pan, Y.-S. Hu, L. Chen, *Energy Environ. Sci.* **2013**, *6*, 2338; c) Y. Fang, L. Xiao, Z. Chen, X. Ai, Y. Cao, H. Yang, *Electrochem. Energy Rev.* **2018**, *1*, 294.

[3] a) S. Y. Hong, Y. Kim, Y. Park, A. Choi, N.-S. Choi, K. T. Lee, *Energy Environ. Sci.* **2013**, *6*, 2067; b) D. Kundu, E. Talaie, V. Duffort, L. F. Nazar, *Angew. Chem., Int. Ed.* **2015**, *54*, 3431; c) N. Yabuuchi, K. Kubota, M. Dahbi, S. Komaba, *Chem. Rev.* **2014**, *114*, 11636.

[4] a) S.-W. Kim, D.-H. Seo, X. Ma, G. Ceder, K. Kang, *Adv. Energy. Mater.* **2012**, *2*, 710; b) B. L. Ellis, L. F. Nazar, *Curr. Opin. Solid State Mater. Sci.* **2012**, *16*, 168; c) V. Palomares, M. Casas-Cabanas, E. Castillo-Martínez, M. H. Han, T. Rojo, *Energy Environ. Sci.* **2013**, *6*, 2312; d) T. Wang, D. Su, D. Shanmukaraj, T. Rojo, M. Armand, G. Wang, *Electrochem. Energy Rev.* **2018**, *1*, 200.

[5] a) R. C. Asher, *J. Inorg. Nucl. Chem.* **1959**, *10*, 238; b) D. P. DiVincenzo, E. J. Mele, *Phys. Rev. B* **1984**, *29*, 1685; c) P. Ge, M. Fouletier, *Solid State Ionics* **1988**, *28–30*, 1172; d) K. Nobuhara, H. Nakayama, M. Nose, S. Nakanishi, H. Iba, *J. Power Sources* **2013**, *243*, 585.

[6] a) W. Xiao, Q. Sun, J. Liu, B. Xiao, P.-A. Glans, J. Li, R. Li, J. Guo, W. Yang, T.-K. Sham, X. Sun, *Nano Res.* **2017**, *10*, 4378; b) W. Xiao, Q. Sun, J. Liu, B. Xiao, Y. Liu, P.-A. Glans, J. Li, R. Li, X. Li, J. Guo, W. Yang, T.-K. Sham, X. Sun, *Nano Energy* **2019**, *66*, 104177.

[7] a) D. A. Stevens, J. R. Dahn, *J. Electrochem. Soc.* **2000**, *147*, 1271; b) P. Thomas, D. Billaud, *Electrochim. Acta* **2002**, *47*, 3303; c) R. Alcántara, F. J. F. Madrigal, P. Lavela, J. L. Tirado, J. M. J. Mateos, C. G. d. Salazar, R. Stoyanova, E. Zhecheva, *Carbon* **2001**, *38*, 1031; d) R. Alcántara, J. M. Jiménez Mateos, J. L. Tirado, *J. Electrochem. Soc.* **2002**, *149*, A201; e) R. Alcántara, J. M. Jiménez-Mateos, P. Lavela, J. L. Tirado, *Electrochem. Commun.* **2001**, *3*, 639; f) R. Alcántara, P. Lavela, G. F. Ortiz, J. L. Tirado, *Electrochem. Solid-State Lett.* **2005**, *8*, A222; g) Y. Li, Y.-S. Hu, X. Qi, X. Rong, H. Li, X. Huang, L. Chen, *Energy Storage Mater.* **2016**, *5*, 191; h) H. Li, F. Shen, W. Luo, J. Dai, X. Han, Y. Chen, Y. Yao, H. Zhu, K. Fu, E. Hitz, L. Hu, *ACS Appl. Mater. Interfaces* **2016**, *8*, 2204; i) P. Liu, Y. Li, Y.-S. Hu, H. Li, L. Chen, X. Huang, *J. Mater. Chem. A* **2016**, *4*, 13046.

[8] a) W. Luo, J. Schardt, C. Bommier, B. Wang, J. Razink, J. Simonsen, X. Ji, *J. Mater. Chem. A* **2013**, *1*, 10662; b) W. Li, L. Zeng, Z. Yang, L. Gu, J. Wang, X. Liu, J. Cheng, Y. Yu, *Nanoscale* **2014**, *6*, 693; c) H. Hou, C. E. Banks, M. Jing, Y. Zhang, X. Ji, *Adv. Mater.* **2015**, *27*, 7861; d) W. Li, M. Zhou, H. Li, K. Wang, S. Cheng, K. Jiang, *Energy Environ. Sci.* **2015**, *8*, 2916.

[9] a) Q. Xia, W. Li, Z. Miao, S. Chou, H. Liu, *Nano Res.* **2017**, *10*, 4055; b) F. Yang, H. Gao, J. Chen, Z. Guo, *Small* **2017**, *1*, 1700216; c) Y. Fu, Q. Wei, G. Zhang, S. Sun, *Adv. Energy Mater.* **2018**, *8*, 1703058; d) Y. Kim, K. H. Ha, S. M. Oh, K. T. Lee, *Chem. - Eur. J.* **2014**, *20*, 11980; e) C. M. Park, H. J. Sohn, *Adv. Mater.* **2007**, *19*, 2465; f) J. Qian, D. Qiao, X. Ai, Y. Cao, H. Yang, *Chem. Commun.* **2012**, *48*, 8931; g) J. Qian, X. Wu, Y. Cao, X. Ai, H. Yang, *Angew. Chem., Int. Ed.* **2013**, *52*, 4633.

[10] L. Wang, X. He, J. Li, W. Sun, J. Gao, J. Guo, C. Jiang, *Angew. Chem., Int. Ed.* **2012**, *51*, 9034.

[11] P. Extance, S. R. Elliott, *Philos. Mag. B* **1981**, *43*, 469.

[12] a) Y. Kim, Y. Park, A. Choi, N. S. Choi, J. Kim, J. Lee, J. H. Ryu, S. M. Oh, K. T. Lee, *Adv. Mater.* **2013**, *25*, 3045; b) W. J. Li, S. L. Chou, J. Z. Wang, H. K. Liu, S. X. Dou, *Nano Lett.* **2013**, *13*, 5480; c) W.-J. Li, S.-L. Chou, J.-Z. Wang, H.-K. Liu, S.-X. Dou, *J. Mater. Chem. A* **2015**, *4*, 505; d) J. Sun, H. W. Lee, M. Pasta, H. Yuan, G. Zheng, Y. Sun, Y. Li, Y. Cui, *Nat. Nanotechnol.* **2015**, *10*,

980; e) Z. Yu, J. Song, M. L. Gordin, R. Yi, D. Tang, D. Wang, *Adv. Sci.* **2015**, *2*, 1400020; f) G.-H. Lee, M. R. Jo, K. Zhang, Y.-M. Kang, *J. Mater. Chem. A* **2017**, *5*, 3683; g) J. Sun, H.-W. Lee, M. Pasta, Y. Sun, W. Liu, Y. Li, H. R. Lee, N. Liu, Y. Cui, *Energy Storage Mater.* **2016**, *4*, 130; h) G. L. Xu, Z. Chen, G. Zhong, Y. Liu, Y. Yang, T. Ma, Y. Ren, X. Zuo, X. Wu, X. Zhang, K. Amine, *Nano Lett.* **2016**, *16*, 3955; i) Y. Wang, L. Tian, Z. Yao, F. Li, S. Li, S. Ye, *Electrochim. Acta* **2015**, *163*, 71; j) W. Li, Z. Yang, Y. Jiang, Z. Yu, L. Gu, Y. Yu, *Carbon* **2014**, *78*, 455; k) B. Ruan, J. Wang, D. Shi, Y. Xu, S. Chou, H. Liu, J. Wang, *J. Mater. Chem. A* **2015**, *3*, 19011; l) Y. Zhu, Y. Wen, X. Fan, T. Gao, F. Han, C. Luo, S.-C. Liou, C. Wang, *ACS Nano* **2015**, *9*, 3254; m) W. Li, Z. Yang, M. Li, Y. Jiang, X. Wei, X. Zhong, L. Gu, Y. Yu, *Nano Lett.* **2016**, *16*, 1546; n) W. Li, S. Hu, X. Luo, Z. Li, X. Sun, M. Li, F. Liu, Y. Yu, *Adv. Mater.* **2017**, *29*, 1605820; o) C. Zhang, X. Wang, Q. Liang, X. Liu, Q. Weng, J. Liu, Y. Yang, Z. Dai, K. Ding, Y. Bando, J. Tang, D. Golberg, *Nano Lett.* **2016**, *16*, 2054; p) H. Gao, T. Zhou, Y. Zheng, Y. Liu, J. Chen, H. Liu, Z. Guo, *Adv. Energy Mater.* **2016**, *6*, 1601037; q) Y. Kim, Y. Kim, A. Choi, S. Woo, D. Mok, N. S. Choi, Y. S. Jung, J. H. Ryu, S. M. Oh, K. T. Lee, *Adv. Mater.* **2014**, *26*, 4139; r) J. Qian, Y. Xiong, Y. Cao, X. Ai, H. Yang, *Nano Lett.* **2014**, *14*, 1865; s) N.-S. Choi, J. Y. Jang, Y.-W. Lee, Y. Kim, J. Lee, S.-M. Lee, K. T. Lee, *J. Mater. Chem. A* **2015**, *3*, 8332; t) Q. Li, Z. Li, Z. Zhang, C. Li, J. Ma, C. Wang, X. Ge, S. Dong, L. Yin, *Adv. Energy Mater.* **2016**, *6*, 1600376; u) J. Liu, P. Kopold, C. Wu, P. A. v. Aken, J. Maier, Y. Yu, *Energy Environ. Sci.* **2015**, *8*, 3531; v) X. Fan, J. Mao, Y. Zhu, C. Luo, L. Suo, T. Gao, F. Han, S.-C. Liou, C. Wang, *Adv. Energy Mater.* **2015**, *5*, 1500174; w) W. Li, L. Ke, Y. Wei, S. Guo, L. Gan, H. Li, T. Zhai, H. Zhou, *J. Mater. Chem. A* **2017**, *5*, 4413; x) W.-J. Li, S.-L. Chou, J.-Z. Wang, H.-K. Liu, S.-X. Dou, *Chem. Commun.* **2015**, *51*, 3682; y) F. Zhao, N. Han, W. Huang, J. Li, H. Ye, F. Chen, Y. Li, *J. Mater. Chem. A* **2015**, *3*, 21754; z) C. Wu, P. Kopold, P. A. van Aken, J. Maier, Y. Yu, *Adv. Mater.* **2016**, *29*, 1604015; aa) S. Liu, J. Feng, X. Bian, J. Liu, H. Xu, Y. An, *Energy Environ. Sci.* **2017**, *10*, 1222; ab) S.-O. Kim, A. Manthiram, *Chem. Mater.* **2016**, *28*, 5935.

[13] X. Li, G. Chen, Z. Le, X. Li, P. Nie, X. Liu, P. Xu, H. B. Wu, Z. Liu, Y. Lu, *Nano Energy* **2019**, *59*, 464.

[14] X. Jiao, Y. Liu, B. Li, W. Zhang, C. He, C. Zhang, Z. Yu, T. Gao, J. Song, *Carbon* **2019**, *148*, 518.

[15] X. Jiao, Y. Liu, T. Li, C. Zhang, X. Xu, O. Kapitanova, C. He, B. Li, S. Xiong, J. Song, *ACS Appl. Mater. Interfaces* **2019**, *11*, 30858.

[16] H. Liu, S. Zhang, Q. Zhu, B. Cao, P. Zhang, N. Sun, B. Xu, F. Wu, R. Chen, *J. Mater. Chem. A* **2019**, *7*, 11205.

[17] T. Yuan, J. Ruan, C. Peng, H. Sun, Y. Pang, J. Yang, Z.-F. Ma, S. Zheng, *Energy Storage Mater.* **2018**, *13*, 267.

[18] X. Liang, C. Chang, W. Guo, X. Jiang, C. Xiong, X. Pu, *ChemElectroChem* **2019**, *6*, 5721.

[19] Y. Wu, Z. Liu, X. Zhong, X. Cheng, Z. Fan, Y. Yu, *Small* **2018**, *14*, 1703472.

[20] B. Liu, Q. Zhang, L. Li, Z. Jin, C. Wang, L. Zhang, Z.-M. Su, *ACS Nano* **2019**, *13*, 13513.

[21] W. Tian, L. Wang, K. Huo, X. He, *J. Power Sources* **2019**, *430*, 60.

[22] a) W. Zhang, M. Dahbi, S. Komaba, *Curr. Opin. Chem. Eng.* **2016**, *13*, 36; b) S. L. Chou, Y. Pan, J. Z. Wang, H. K. Liu, S. X. Dou, *Phys. Chem. Chem. Phys.* **2014**, *16*, 20347.

[23] J. Song, Z. Yu, M. L. Gordin, S. Hu, R. Yi, D. Tang, T. Walter, M. Regula, D. Choi, X. Li, A. Manivannan, D. Wang, *Nano Lett.* **2014**, *14*, 6329.

[24] W. Xiao, Q. Sun, M. N. Banis, B. Wang, J. Liang, A. Lushington, R. Li, X. Li, T.-K. Sham, X. Sun, *ACS Appl. Mater. Interfaces* **2019**, *11*, 30763.

[25] a) N. Nitta, D. Lei, H. R. Jung, D. Gordon, E. Zhao, G. Gresham, J. Cai, I. Luzinov, G. Yushin, *ACS Appl. Mater. Interfaces* **2016**, *8*, 25991; b) J. Song, Z. Yu, M. L. Gordin, X. Li, H. Peng, D. Wang, *ACS Nano* **2015**, *9*, 11933.

[26] a) X. Liu, W. Yang, Z. Liu, *Adv. Mater.* **2014**, *26*, 7710; b) J. Nelson Weker, M. F. Toney, *Adv. Funct. Mater.* **2015**, *25*, 1622.

[27] a) S. Wan, A. K. Tieu, Q. Zhu, H. Zhu, S. Cui, D. R. Mitchell, C. Kong, B. Cowie, J. A. Denman, R. Liu, *Sci. Rep.* **2016**, *6*, 26008; b) Z. Yin, M. Kasrai, G. M. Bancroft, K. H. Tan, X. Feng, *Phys. Rev. B* **1995**, *51*, 742.

[28] a) N. Yabuuchi, Y. Matsuura, T. Ishikawa, S. Kuze, J.-Y. Son, Y.-T. Cui, H. Oji, S. Komaba, *ChemElectroChem* **2014**, *1*, 580; b) Y. Zhang, H. Wang, Z. Luo, H. T. Tan, B. Li, S. Sun, Z. Li, Y. Zong, Z. J. Xu, Y. Yang, K. A. Khor, Q. Yan, *Adv. Energy Mater.* **2016**, *6*, 1600453.

[29] a) J. Zhou, X. Liu, W. Cai, Y. Zhu, J. Liang, K. Zhang, Y. Lan, Z. Jiang, G. Wang, Y. Qian, *Adv. Mater.* **2017**, *29*, 1700214; b) Y. Zhang, X. Rui, Y. Tang, Y. Liu, J. Wei, S. Chen, W. R. Leow, W. Li, Y. Liu, J. Deng, B. Ma, Q. Yan, X. Chen, *Adv. Energy Mater.* **2016**, *6*, 1502409.

[30] R. B. Diegle, N. R. Sorensen, C. R. Clayton, M. A. Helfand, Y. C. Yu, *J. Electrochem. Soc.* **1988**, *135*, 1085.

[31] Q. Xiao, X. Cui, Y. Shi, Y. Hu, T.-K. Sham, H. Piao, J. McMahon, *Can. J. Chem.* **2015**, *93*, 113.